



Optical readout and actuation of plasmonic nano-optomechanical drum resonators

JENTE VANDERSMISSEN,¹ RANDY A. MEIJER,^{1,2} JOHNEPH SUKHAM,¹ ALOYS ERKELENS,¹ JAN BONNE AANS,^{1,3} AND EWOLD VERHAGEN^{1,*} 

¹Center for Nanophotonics, AMOLF, Science Park 104, 1098 XG, Amsterdam, The Netherlands

²Currently with Advanced Research Center for Nanolithography (ARCNL), Science Park 106, 1098 XG, Amsterdam, The Netherlands

³Currently with Department of Physics, Utrecht University, Leonard S. Ornstein Laboratory, Princetonplein 1, 3584 CC Utrecht, The Netherlands

*verhagen@amolf.nl

Abstract: We demonstrate optical readout and actuation of nanomechanical motion using plasmonic fields in a nanoscale gap waveguide. The top gold layer of the waveguide is free to vibrate like a drumhead, and patterned with an optical grating to facilitate efficient coupling to free-space radiation. The change of the plasmonic gap mode with the top layer position couples the plasmonic resonance to the mechanical displacement of the drum. We characterize optical and mechanical resonances of the system, and demonstrate sensing of nanomechanical vibrations with $\sim 10^{-14}$ m/ $\sqrt{\text{Hz}}$ sensitivity. The mechanical resonators are actuated through plasmonic forces. Quantifying their magnitude shows that plasmonic forces can significantly exceed pure radiation pressure, indicating that their nature is dominated by a photothermoelastic effect. This work opens avenues to the use of plasmonic readout and control in nanomechanical sensing applications.

© 2023 Optica Publishing Group under the terms of the [Optica Open Access Publishing Agreement](#)

1. Introduction

Nano-opto-electro-mechanical systems (NOEMS) couple mechanical degrees of freedom to optical and electrical fields in on-chip architectures [1]. Those fields provide means to both probe and control mechanical motion at the nanoscale, with interesting applications from optical switching to coherent signal transduction. They are of particular interest to sensing applications [2–9] as miniaturized NOEMS have proven to be very sensitive to small perturbations in displacement [10,11], mass [12], temperature [13,14], and force [15,16]. Cavity optomechanical devices are a class of systems where optical resonator fields are coupled to a mechanical resonator [17]. This allows for highly efficient displacement measurement, as well as actuation of mechanical motion through radiation pressure forces [17–26].

Typical optomechanical sensors employ dielectric or mirror-based cavities and are thus constrained by the diffraction limit, which limits optical mode confinement to scales of at least the optical wavelength. The diffraction limit presents an effective limitation to optomechanical design: On the one hand, the optomechanical frequency shift $G = \partial\omega_c/\partial x$ of cavity frequency ω_c due to displacement x as well as the force $\hbar G$ exerted on the mechanical resonator per photon are inversely proportional to cavity size. On the other hand the spatial extent of nanomechanical resonators can be significantly smaller in one or more dimensions than the optical wavelength. While sensitivity can be boosted by employing high optical quality factors, the associated narrow optical linewidths can present practical disadvantages. For nanoscale sensors, in particular with the perspective of large-scale integration and massively parallel implementation [27], it could thus be useful to pursue alternative approaches to optomechanical transduction that are inherently broadband and efficiently interfaced to optical input and output fields.

Plasmonic optomechanical devices have been explored as optically broadband systems for mechanical transduction, exploiting their ability to confine light to subwavelength dimensions to feature large optomechanical interaction strengths and natural integration with nanomechanical resonators [28–32]. Plasmonic systems have been used extensively in the study of small-scale perturbations [33,34] and were recently also exploited in reconfigurable metamaterials [35–38], for motion sensing [28,30,39,40], as switches [41], for photothermal studies [42] and as strain sensors [43]. Forces between plasmonic particles and in plasmonic structures have been studied in a variety of systems, ranging from metamaterials [37,44–47], nanoantennae [48,49], and plasmonic tweezers [50–55], to nanomechanical systems [31,56,57]. Besides measurement, plasmonic fields could also provide an interesting pathway to the actuation of sensors, of high interest to various sensing applications [10]. Plasmon-induced mechanical self-oscillation was observed [29,31], and Ou et al. used forces exerted by plasmonic fields to actuate string-like mechanical motion [37], reporting forces of the order of $0.5 P/c$, with P the incident power and c the speed of light. While the latter study reported forces that could be explained purely from the Maxwell stress tensor, other works have considered thermal effects in actuation mechanisms [29,31,46].

In this work, we report a plasmonic optomechanical system with a large overlap between nano-confined light fields and the displacement of a nanomechanical resonator's surface, and study both transduction and actuation of motion. The system is based on a plasmonic gap waveguide (also called metal-insulator-metal waveguide), which confines light in between two metal surfaces separated by a nanoscale gap. These plasmonic fields feature strong sensitivity to a small perturbation of the gap [58]. We fabricate gap waveguides with a top metal film that can move freely as a drum, as illustrated in Fig. 1. The top metal layer is suspended by partially

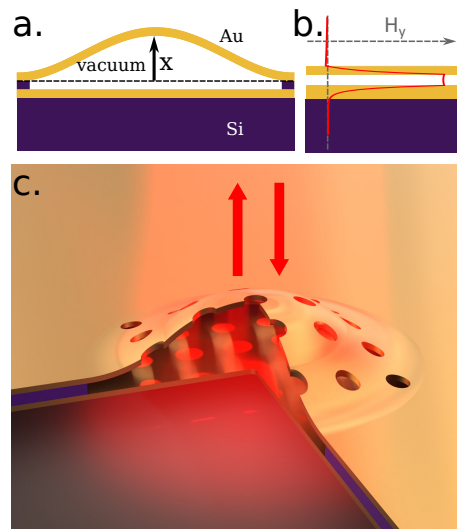


Fig. 1. Plasmonic optomechanical gap resonator. (a) The displacement associated with the motion of one of the mechanical modes of the Au drum is described using a parameter x . Depicted here is the fundamental mode of the drum. (b) The in-plane component of the magnetic field of the surface plasmon gap mode that is confined between the metal layers. There is a strong field in the vacuum gap, which is affected by a change of the separation of the Au layers. (c) Artistic representation of the system under study. It consists of two thinly spaced metal layers, where the top layer is free to move and has an optical grating that couples gap plasmons to free-space radiation. The motion of the top membrane is read out and actuated via the gap plasmons.

etching away a Si sacrificial layer, leaving a suspended membrane. It is patterned with a grating of subwavelength holes in order to facilitate optical coupling of free-space light to the plasmonic mode. This provides advantages for device integration, since the device can be addressed through free-space laser fields, without the need for electrical leads or on-chip waveguides, which could enable a denser packing of devices to be used as sensors.

The motion of the drum is coupled to the plasmonic fields in the MIM waveguide. The grating in the top film creates an optical resonance for normal-incidence light, whose properties are affected by the displacement of the membrane resonator. This coupling allows the MHz-frequency motion to be transduced to optical modulations of a near-infrared laser that is probing the resonance. Moreover, we report controlled actuation of the motion via an optical pump and measure the force exerted by the plasmonic field on the mechanical drum modes. We find that it is approximately 100 times greater than what is predicted by the Maxwell stress tensor and the optomechanical frequency shift, suggesting that photothermal forces can be important in nanoplasmonic devices and could in fact play an enabling role in sensing applications.

2. Materials & methods

2.1. Fabrication

For the fabrication of the drum resonators, a triple layer stack of Au, a-Si as a sacrificial layer, and Au is evaporated on a silicon substrate. A Ge spacer layer of 1.5 nm thickness is evaporated in between both gold layers and the silicon sacrificial layer, to minimize migration of Si into the Au lattice. A Ti adhesion layer of 1.5 nm is placed between the silicon substrate and the bottom gold layer. The system used for deposition is a Polyteknik Flextura M508 E, in which the materials are deposited at a rate of 0.5 Å/s. The bottom gold layer has a thickness of 100 nm and the top membrane layer has a thickness of 60 nm. The Si spacer, which determines the gap size, has a thickness of 80 nm.

Using a focused ion beam (FIB, FEI Helios), holes are milled into the top layer. These holes function as both an access to the sacrificial Si layer for etching, and as an optical grating to allow coupling of light to the plasmon mode. Subsequently, the sacrificial layer is removed using a XeF₂ dry etch step in the same system. Etching times are chosen with the aim to remove all material in between the holes, fully releasing a drum that is supported by the remaining silicon film outside the patterned area. The XeF₂ etch is isotropic, and found to extend ~750 nm outside the edges of the holes. The shape of the drum is thus determined by the pattern of holes in the top film and the underetch. For a square arrangement of holes the drum shape is indeed largely square, whereas for other patterns it resembles an octagon. The hole pattern is determined by fitting an optimum number of holes fully within a circle with the desired radius (minus the underetch depth). We did not note a correlation between hole pattern shape and observed mechanical quality factors.

We note that the FIB milling implants Ga⁺ ions into the silicon film. As we detail in [Supplement 1](#) section 7, this can leave small ‘pads’ of Ga-containing material that are not fully removed by the XeF₂ etch right underneath the holes. They are not found to significantly impact the plasmonic properties. The fabrication process, as well as scanning electron microscopy (SEM) images of example devices, is outlined in Fig. 2. We have noticed that releasing a drum with a radius of ~6 μm or larger causes the drum to collapse. This could potentially be mitigated by engineering the top layer to exhibit tensile strain, which could be done by e.g. sputtering aluminium.

2.2. Measurement setup

The setup that is used for optical readout and actuation is shown in Fig. 3. A variable wavelength probe laser (Toptica CTL, 1460-1570 nm), is used to measure the drum’s reflectance. The probe laser wavelength can be tuned to optimise the signal from the structure under study. The sample

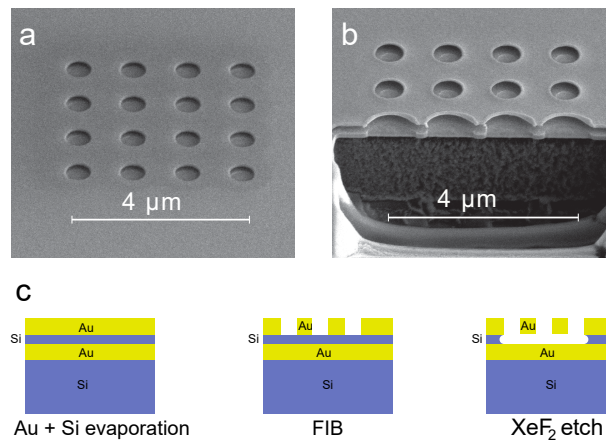


Fig. 2. (a) An example of a fabricated plasmonic drum resonator. The holes made through FIB are visible and the top layer is suspended. (b) A crosscut of the same drum, showing the suspension of the top layer after successful under-etching of the Si sacrificial layer. (c) Overview of the fabrication process. We start with evaporation of the Au, the Si sacrificial layer, and the adhesion layers (left). Subsequently, holes are created in the top gold layer through FIB (middle), and lastly the top layer is released by dry etching the Si sacrificial layer.

is placed inside a vacuum chamber, which is pumped down to approximately 10^{-3} mbar. Light is focused on the sample using a Mitutoyo MY20X-824 objective (0.40 NA), giving spot size of approximately $3 \mu\text{m}$. This value is obtained by scanning the laser spot over the edge of a large square hole milled into the gold layers and observing the reflected power. A curve is subsequently fitted to the position-dependent reflectivity to estimate the diameter of the Gaussian focus.

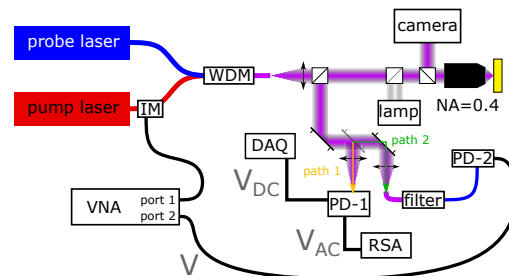


Fig. 3. The setup used for actuation and readout of the motion. The greyed out mirror before detector PD-1 can be added or removed from the setup, where adding it will lead to path 1 being followed, and subsequently hitting detector PD-1. If the mirror is not added, path 2 is followed, and the beam is coupled to a fiber that leads to detector PD-2. The different voltages resulting from the detectors are denoted in grey, using the same nomenclature as in the rest of the text. The sample is indicated in yellow.

Light reflected from the sample is focused on one of two detectors, selected via a removable mirror. The first is an AC-coupled fast photodiode (Newport 1811-FC-AC, denoted PD-1). The second path is focused on an optical fiber, which contains a wavelength filter that transmits the probe laser light, before being detected on a DC-coupled photodiode (Newport 1811-FC, denoted PD-2). A sketch of the setup is displayed in Fig. 3. The choice of detector depends on the experiment that is conducted, as we describe below.

As the drum moves, the properties of the optical cavity, and hence its normal-incidence reflectance R , vary with the drum's displacement x . The thermal motion of the drum is thus transduced through the optical reflectance. We can generally state that

$$P_{\text{out}}(x) = R(x)P_{\text{in}}, \quad (1a)$$

$$S_{PP} = \left(\frac{\partial R}{\partial x} \right)^2 P_{\text{in}}^2 S_{xx}, \quad (1b)$$

where P_{in} is the input power of the laser, P_{out} the reflected power, modulated by the motion, and S_{xx} and S_{PP} the (two-sided) displacement spectral density of the resonator and the power spectral density of the reflected light, respectively. The recorded voltage by detector PD- i ($i = 1, 2$) is $V_i = \zeta_i P_{\text{out}}$ where ζ_i is the detector-specific transduction factor (in V/W). This transduction factor accounts for the transmission through the optical detection path, as well as for the responsivity and amplification of the detector. It does not take into account the transmittance of the optical filter in the second path, which we denote separately by ζ_{filter} .

The DC voltage of detector PD-1, containing time-averaged information about the drum reflectance, is led to a National Instruments data acquisition device (DAQ). The AC voltage of the same detector, which transduces the mechanical motion of the drum, is connected to a Tektronix RSA306B real-time spectrum analyser (RSA).

By using a fiber-coupled intensity modulator (IM), a pump laser at 1550 nm can be used to actuate the motion of the structure. For those experiments, the pump laser is combined with the probe laser in a fiber coupler (WDM, wavelength division multiplexer) such that both can be focused to the sample simultaneously. The reflected signal from the probe laser is led to PD-2 via path 2 (Fig. 3), where the pump laser is filtered out using an optical filter. The linear response of the mechanical system is studied by use of a vector network analyser (VNA). The output V_1 from port 1 of the VNA provides the modulation frequency for the IM. The voltage V_2 coming from PD-2, containing information about the motion, serves as input for port 2 of the VNA. The transfer parameter $S_{21} \equiv V_2/V_1$ of the VNA contains the information about the linear response of the system to the applied signal. This is explained further in section 3.2.3.

3. Results

3.1. Simulated optical and mechanical properties of the resonators

The gap plasmons are coupled to free-space radiation through diffraction at a periodic array of subwavelength holes in the top layer. This creates a resonant optical response if the in-plane wavevector of a diffracted order matches the wavevector magnitude k_{SPP} of the gap plasmon polariton, i.e., if

$$k_{\text{SPP}} = \left| \mathbf{k}_{\parallel} + n \frac{2\pi}{a} \hat{\mathbf{x}}_k + m \frac{2\pi}{a} \hat{\mathbf{y}}_k \right|, \quad (2)$$

where \mathbf{k}_{\parallel} is the in-plane component of the incident wavevector, n and m are integers specifying the diffraction orders of the square grating, $\hat{\mathbf{x}}_k$ and $\hat{\mathbf{y}}_k$ are unit vectors, and a is the grating pitch in both directions. This equation is of course valid for an infinitely periodic grating, whereas our devices have only a small number of holes. Nonetheless, we expect that the basic diffraction mechanism is similar.

To understand the mechanism better and determine useful parameters, we therefore study simulations of the optical response of an infinite lattice of holes in the top membrane using COMSOL Multiphysics 5.2a (see Supplement 1 section 1 for details on the simulation methods). Figure 4(a) shows the calculated reflectance of a plane wave from the structure with a 1.15 μm period and 500 nm hole diameter as a function of frequency and in-plane wavevector k , around the frequencies that satisfy Eq. (2) for normal incidence. We recognize multiple crossing bands

appearing as reduced reflectance in the spectrum, associated with diffraction to surface plasmon modes in a square lattice [59]. The ‘brightness’ of the bands, i.e., the efficiency with which they couple to free-space radiation, varies. At $k = 0$, we see that the spectrum is characterized by a single resonance dip, with reflection on resonance becoming very small (~ 0.1) for the chosen hole diameter. The general design of a gap waveguide with perforated top plate is indeed known to allow near-perfect absorption [60]. As we detail in [Supplement 1](#) section 2, the hole diameter can be chosen to minimize reflectance without introducing unnecessarily large linewidth due to increased radiation at large hole sizes. Larger hole diameters increase the rate at which the plasmonic gap mode is coupled to the free-space radiation through diffraction. Near-zero reflectance is reached for critical coupling, i.e. when the outcoupling rate is equal to the absorption rate. While the absorption rate also changes slightly due to the presence of the holes, the fact that the reflectance can approach zero for a proper hole diameter shows that the critical coupling condition can be met. The optical frequency and decay rates at $k = 0$, with k being the in-plane wave vector, vary furthermore with grating pitch and with separation distance x between the metal layers. Figures 4(a) and (b) compare the spectra for metal layer separations of 80 and 100 nm, respectively. It is this change of optical reflectance with membrane displacement x that allows optical transduction of mechanical motion.

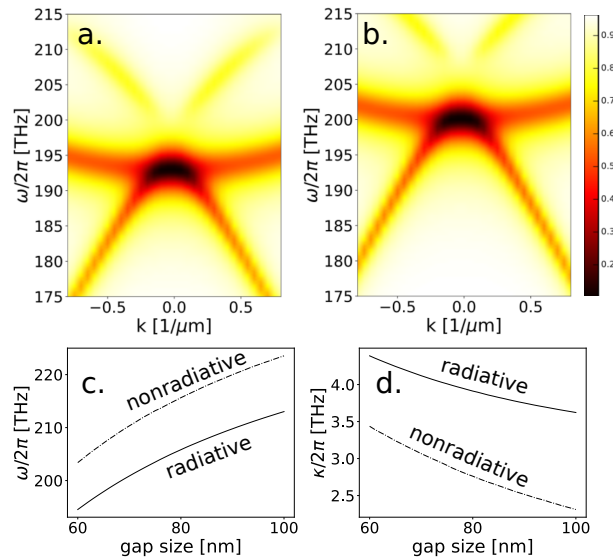


Fig. 4. (a,b) Simulated angle-dependent reflectance spectra of an infinite two-dimensional lattice of holes in the top layer of a plasmonic gap waveguide. The square lattice under study has a hole pitch of $1.15 \mu\text{m}$ and a hole diameter of 500 nm . The gap thickness is 80 nm (a) and 100 nm (b), and the reflectance for s and p polarizations are averaged. (c,d) The variation of the optical resonance frequency (c) and optical decay rate (d) with x for $k = 0$, obtained from simulations of the quasinormal modes of a waveguide. The two eigenmodes are labeled ‘radiative’ and ‘nonradiative’ and correspond to bright and dark bands, respectively, distinguished by their linewidth.

Using the COMSOL eigenvalue solver including perfectly matched layer (open) boundary condition to the top, we can obtain the expected frequency and linewidth of the surface plasmon modes from the complex eigenfrequency of the obtained quasinormal modes. [Supplement 1](#) section 1 provides details on the simulation methods. The optical frequency and decay rate κ are plotted as a function of layer separation for the modes at $k = 0$ in Figs. 4(c) and (d), respectively.

We notice that the derivative of the cavity frequency to x becomes greater with decreasing separation, while there is also a modest increase of the linewidth of the radiative mode of interest.

Given that at $k = 0$ only a single resonance is seen, we describe the optical reflectance of the grating for normal incidence as

$$R = \left| r_0 e^{i\varphi} - \frac{\kappa_{\text{ex}}}{\kappa/2 - i\Delta} \right|^2 = r_0^2 - \frac{\kappa_{\text{ex}}}{\kappa^2/4 + \Delta^2} (r_0 (\kappa \cos \varphi + 2\Delta \sin \varphi) - \kappa_{\text{ex}}), \quad (3)$$

where $1 - |r_0|^2$ is scattering loss and φ is a possible phase difference of the resonantly reflected field and the direct reflection. The plasmonic resonance is thus modeled as a Lorentzian oscillator whose spectrum can in principle feature a Fano-like lineshape. The total decay rate κ is the sum of κ_{ex} , the optical coupling rate to the laser beam, and κ_0 , the internal optical decay rate including absorption. The optical detuning $\Delta = \omega - \omega_c$ gives the difference between the laser frequency ω and the optical cavity frequency ω_c . We consider that the parameters Δ , κ_0 , and κ_{ex} could in principle each depend linearly on the displacement x of the top layer, such that

$$\frac{\partial R}{\partial x} = \frac{\partial R}{\partial \omega_c} \frac{\partial \omega_c}{\partial x} + \frac{\partial R}{\partial \kappa_0} \frac{\partial \kappa_0}{\partial x} + \frac{\partial R}{\partial \kappa_{\text{ex}}} \frac{\partial \kappa_{\text{ex}}}{\partial x}. \quad (4)$$

The dominant contribution in the simulated structures comes from the first term, i.e. dispersive coupling due to $\partial \omega_c / \partial x$. The magnitude of the optomechanical frequency shift is $\partial \omega_c / \partial x / (2\pi) = 418$ GHz/nm for a gap of 80 nm, and varies quite strongly with the gap size: For 90 nm gap $\partial \omega_c / \partial x / (2\pi) = 353$ GHz/nm and for 70 nm gap $\partial \omega_c / \partial x / (2\pi) = 503$ GHz/nm. In contrast, the expected linewidth shift $\partial \kappa / \partial x / (2\pi)$ in Fig. 4(d) is approximately 20 GHz/nm, and varies comparatively less with gap size. We return to the possible variation of both κ_0 and κ_{ex} with displacement in section 3.2.2. For a shot-noise limited measurement of displacement, the signal-to-noise ratio (SNR) scales as $(\partial R / \partial x)^2 P_{\text{in}}$ when employing direct detection of reflected intensity. This means that, for sensing purposes, it is generally desirable to use a small gap, since the stronger responsivity of the optical resonance to mechanical perturbations for small gaps outweighs the detrimental effect of a larger resonance linewidth, for the parameter regime we consider.

One can estimate the electromagnetic force exerted on the top film with this infinite lattice using the Maxwell stress tensor, given by [61]

$$T = \varepsilon_0 \varepsilon_r \left(\mathbf{E} \otimes \mathbf{E} - \frac{1}{2} |\mathbf{E}|^2 I \right) + \mu_0 \mu_r \left(\mathbf{H} \otimes \mathbf{H} - \frac{1}{2} |\mathbf{H}|^2 I \right), \quad (5)$$

where I is the unit tensor. The resulting force on a volume V is

$$\mathbf{F} = \int_V \nabla \cdot T \, dv = \int_{\partial V} T \cdot \mathbf{n} \, da, \quad (6)$$

where ∂V is the surface enclosing the volume and \mathbf{n} the surface normal vector. We note that this expression neglects the Casimir force, which results from the vacuum field.

Light is simulated to be perpendicularly incident on the grating used in Fig. 4(a), yielding the reflection spectrum shown in Fig. 5(a). Using Eq. (6), the optical force exerted by the bright mode on the membrane is calculated for an incident power P , as shown in Fig. 5(b). As the resonance frequency of the cavity is approached, the force on the structure, forcing the top membrane towards the substrate with magnitude $F \equiv |\mathbf{F}|$, increases. The total force reaches a maximum value of $22.4 P/c$ on resonance, or 76.5 pN for a pump intensity of $1/1.15^2$ mW/ μm^2 .

By calculating the individual contributions to the force of the upper and lower surface of the membrane, we recognize that the former approaches the radiation pressure force $2P/c$ on a flat Au mirror away from resonance, whereas the latter dominates on resonance, due to the enhanced

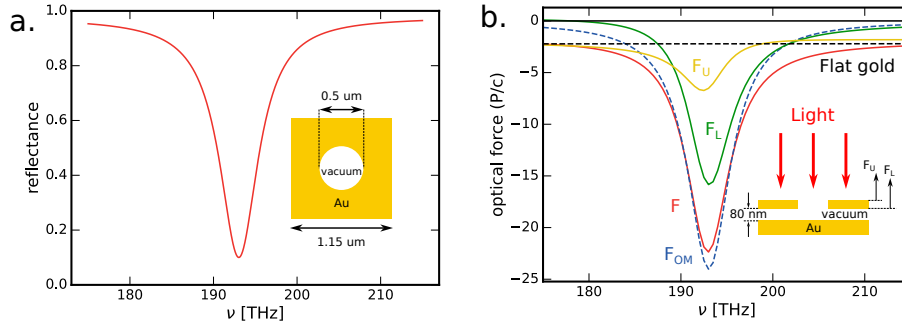


Fig. 5. (a) Reflection spectrum for an infinite lattice of holes in a gold membrane suspended above a gold substrate. The lattice pitch is $1.15 \mu\text{m}$, while the hole diameter is 500 nm . The membrane is suspended 80 nm above the substrate surface. The inset shows the unit cell of this lattice, as seen from the top. (b) Spectral dependence of the force exerted on the top membrane in this infinite lattice for an incident power P . The inset shows a crosscut of the structure. We distinguish between two calculated force contributions; that on the upper surface of the membrane (F_U) and that on the lower surface (F_L). The total force F on the membrane is the sum of these. Also indicated as a black dashed line is the force on an unstructured gold layer, being approximately equal to the radiation pressure on a perfect mirror. With the blue dashed line, the expected optomechanical force F_{OM} due to dispersive coupling is indicated.

field in the gap. We moreover note that the maximum force has a good correlation with the force expected from optomechanical theory $F_{OM} = \hbar G n$, with G the optomechanical dispersive coupling constant and n the cavity occupancy, calculated as $n = \kappa_{\text{ex}} / (\kappa^2/4 + \Delta^2) (P / (\hbar\omega))$. This again confirms that the dispersive optomechanical coupling characterized by frequency shift G dominates the interaction.

We remark that this analysis of a plane wave incident on an infinite grating is a simplified depiction of the actual experiment. With a Gaussian beam incident on the sample, the optical response will effectively be averaged over the angular range that is contained in the incident beam. Effectively, this is expected to lead to a broadening of the spectral resonance. As such, we thus expect a trade-off between the optical resonance linewidth and the size of the drum, which defines the required transverse localization of the optical field. In general, optimal designs would feature a drum size that is comparable to the transverse coherence of the optical field, given by the decay length of the plasmonic mode propagating in the gap waveguide. This, in turn, depends on the size of the holes, as shown in Section 2 of the Supplement 1. Finally, we remark that the finite size of the hole array, as well as the fact that at the edge of the drum there is an interface between vacuum and silicon inside the gap, could lead to spatial optical mode confinement in the plane of the waveguide.

It is expected that the optical field, which exerts an out-of-plane downwards force, couples well to the fundamental mechanical mode of the drum, which displays a large area of membrane displacement in the out-of-plane direction. The simulated displacement of this and several other mechanical modes is shown in Fig. 6. These have been obtained through a mechanical eigenmode study in COMSOL.

It is relevant to determine the effective mass m_{eff} of the mode, which links the (thermal) energy present in a mechanical mode to its mean square displacement $\langle x^2 \rangle$ as

$$\langle E \rangle = k_B T = m_{\text{eff}} \Omega_m^2 \langle x^2 \rangle, \quad (7)$$

where Ω_m is the mechanical mode frequency, T the bath temperature, and we have employed the equipartition theorem [62]. The effective mass is needed to determine the magnitude of the

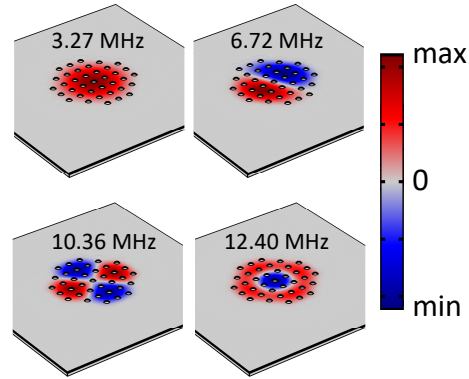


Fig. 6. Theoretical mechanical modes of the microdrum. The out-of-plane displacement is plotted, and the mechanical frequencies of the corresponding modes are indicated in each panel.

displacement spectral density of a mechanical resonator. In thermal equilibrium, this is given by

$$S_{xx}^{\text{th}} = \frac{2k_B T}{m_{\text{eff}}} \frac{\Gamma_m}{(\Omega_m^2 - \Omega^2)^2 + \Gamma_m^2 \Omega^2}, \quad (8)$$

where Γ_m is the mechanical linewidth and the relation

$$\frac{1}{2\pi} \int S_{xx}^{\text{th}} d\Omega = \langle x^2 \rangle \quad (9)$$

holds. Upon defining the displacement x as the maximal displacement within a mechanical mode profile, the effective mass of the mode can be determined via the formula

$$m_{\text{eff}} = \int_V \rho(\mathbf{r}) |\mathbf{u}(\mathbf{r})|^2 d\mathbf{r}, \quad (10)$$

where V is the volume of our moving membrane, ρ is the mass density, and \mathbf{u} is the displacement, normalised to its maximum magnitude. For a perforated gold drum where the radius of the suspended membrane is approximately $4.5 \mu\text{m}$, the effective mass of the fundamental mode (upper left in Fig. 6) is 9.5 pg .

3.2. Experiments

3.2.1. Detecting thermal motion

Figure 7 shows a measured displacement spectrum obtained by measuring the modulation of reflected intensity of a $\sim 4.5 \mu\text{m}$ radius drum using an incident power of $500 \mu\text{W}$. At the used wavelength, the reflectance was significantly reduced and depended on wavelength, indicating that the laser was tuned to the side of a plasmonic resonance. The total signal, as measured by the RSA, consists of several contributions: The electronic noise stems from the amplifier in the detector, whereas the shot noise is related to the quantized nature of the detected optical intensity. The magnitude of its optical power spectral density is $\hbar\omega P_{\text{det}}$, with P_{det} the optical power impinging on the detector. Together, electronic and shot noise provide the imprecision to the total signal. The motion of the resonator is transduced to the signal on the detector through Eq. (1b). In order to obtain the motion spectral density from the RSA power spectrum, the Lorentzian peak area is normalised to $k_B T / (2m_{\text{eff}})$ according to Eq. (7). This calibrates the vertical axis of Fig. 7. The imprecision for this displacement measurement is 1.27×10^{-14}

$m/\sqrt{\text{Hz}}$. The mechanical quality factor, obtained from the Lorentzian fit to the spectrum, is 139 in this measurement, which was found to be a typical value among the investigated drums. As we conclude from pressure-dependent measurements reported in section 8 of the [Supplement 1](#), the quality factor is not limited by gas damping below pressure of ~ 1 mbar; Other mechanisms such as clamping losses, thermoelastic damping, and two-level fluctuators are the possible sources of mechanical dissipation.

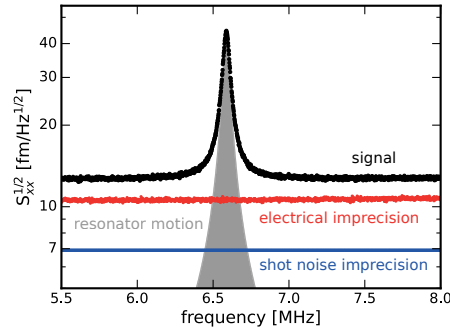


Fig. 7. Spectral displacement density of one of the modes of a drum, with $\Omega_m = 2\pi \times 6.59$ MHz, $Q_m = 139$, and estimated $m_{\text{eff}} = 9.5$ pg. The grey area shows the fitted thermal spectral displacement density of the resonator, and the black curve the measured spectrum, including the imprecision noise 1.61×10^{-28} m²/Hz. This spectrum was obtained using a probe laser with a power of 500 μ W. The red data shows the electronic noise originating from the detector, whereas the blue curve shows the calculated shot noise imprecision. The displacement spectral density of the resonator is depicted as the area shaded grey.

As the probe power is increased, we observe an increase in signal strength. The signal strength has an approximately quadratic dependence on the power, per Eq. (1b) and the fact that $P_{\text{RSA}} = (2.12 \text{ RBW} \zeta_1^2 / Z) S_{PP}$, with RBW the resolution bandwidth of the spectrum analyzer and Z its impedance. Since absorption of the laser light could lead to a local increase of the temperature of the drum resonator, the associated increase of thermal fluctuations could lead to a scaling of the signal with laser power that exceeds a quadratic dependence. This is observed in Fig. 8(b), where several lines assuming different linear dependence of temperature with laser power are compared to the measured signal strengths. We find that a temperature increase of 28 K per mW of incident power best describes the observations. In Fig. 8(a), we also observe a mechanical frequency shift with increasing probe power, which was repeatable and not dependent on fluctuations in the setup. We speculate that this is at least in part due to the heating of the structure. The Young's modulus E_y in the elastic regime is modelled as $E_y = (8.35 \cdot 10^{10} - 2.34 \cdot 10^7 \text{K}^{-1} T) \text{ N/m}^2$ [63]. If the frequency change would be fully ascribed to the change of the Young's modulus, this would predict a temperature rise of 83 K, which is not in line with the observed increase of ~ 14 K in Fig. 8(b). We thus conclude that also other mechanisms could contribute to the frequency shift. We can exclude the possibility that the optical spring effect plays a significant role, from the fact that its magnitude is only predicted to be on the order of a few Hz at maximum given the system parameters [17], and from the fact that we do not observe the dispersive dependence of the shift on laser wavelength that is characteristic for the spring effect. We hypothesize that the reduction of frequency could be associated by a differential thermal expansion of the gold film and the underlying layers, to induce a compressive stress in the film that lowers the frequencies of flexural modes.

Figure 9(a) shows displacement spectral densities for various resonators with differing radii of the suspended membrane, which are indicated per spectrum. The mechanical frequency of

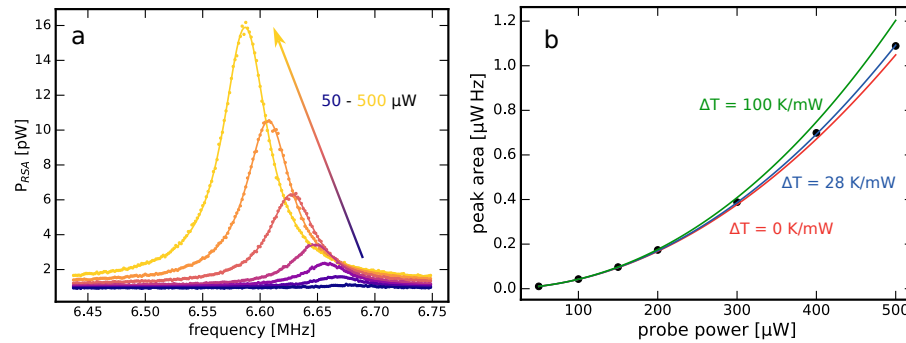


Fig. 8. (a) Recorded optical fluctuation spectra for different probe powers. The increase is approximately quadratic in the probe power. There also occurs a frequency shift for increasing power. (b) Increase of signal strength with probe power. The near-quadratic dependence is readily visible. Three additional lines have been plotted, each of which corresponds to an increase in temperature with probe power. This increase causes a deviation from pure quadratic scaling.

the resonator generally increases as the size of the resonator decreases. As the drum decreases in size, the noise floor also goes up. This can be explained by poorer optical coupling to the mechanical system, since together with a decrease in the drum radius, there is also a decrease in the size of the optical grating. The optomechanical transduction is thus lower. We remark that the indicated diameters are only estimations: since the hole pitch is equal for all drums, the numbers of holes differ from 9 holes for the 2.5 μm drum to 37 holes for the 4.5 μm drum. The actual diameter is determined through the underetch of the holes. We notice that the drum with a radius of 4 μm deviates from the trend in mechanical frequency, and that also its signal strength is lower than expected. This could possibly be due to the drum not being fully suspended, e.g. due to an imperfect underetch of the membrane or an Au grain that connects the top and bottom Au films after release. Another possible source of imperfect release is the material that remains at the bottom of the holes due to Ga implantation of the Si sacrificial layer (see [Supplement 1](#) section 7). Any form of connection would alter the mechanical mode shape which could reduce the coupling to the plasmonic field. While these imperfections are not always seen, it indicates that it would be interesting to investigate alternative fabrication methods, e.g. employing evaporation and lift-off for the top film.

3.2.2. Resonant plasmonic transduction

Evidence for imperfect suspension of drums is also present in some of the mechanical fluctuation spectra. Figure 9(b) shows an example RSA spectrum for a different drum with 4.5 μm radius that features an anharmonic spectrum and multiple resonances at comparable frequencies. The effective mass of these modes of unknown nature can hence not be ascertained, nor can its optomechanical coupling strength be readily estimated. Here, we present a scheme to nonetheless gain information on the optomechanical interaction strength, and specifically the vacuum optomechanical coupling strength g_0 [17], while shedding light on the role of the plasmonic resonance on transduction. We use the strongest peak in the spectrum shown in Fig. 9(b).

Figure 10(a) shows measured optical reflectance as a function of the frequency of a tunable laser, displaying a clear minimum within the laser range. The spectrum is fitted with the single-resonance response Eq. (3) (fit parameters provided in caption). Including a displacement dependence on the three parameters ω_c , κ_{ex} and κ_0 in Eq. (4) allows describing the change in reflectance with displacement, as outlined in [Supplement 1](#) section 6. The fact that they change with layer separation can also be seen from the simulations in Figs. 4(c) and 4(d). A first

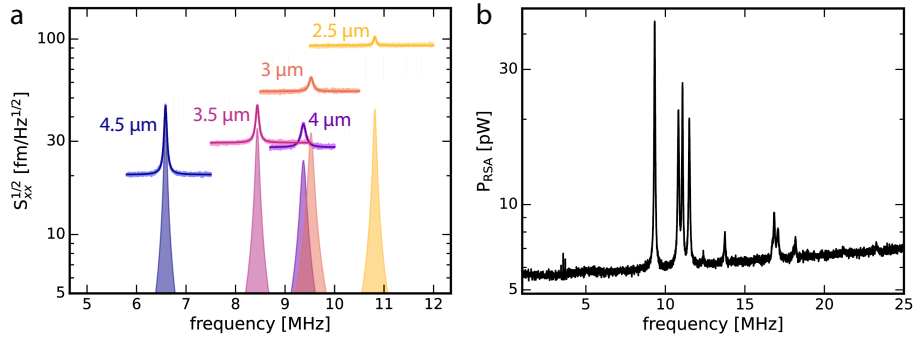


Fig. 9. (a) Displacement spectral density of different resonators. The radius of the resonating membrane is indicated for each spectrum. As the radius of the suspended membrane decreases, the mechanical resonance generally tends to increase. The coloured area shows the background-subtracted spectral density of the resonator, whereas the lines show fits to the measured spectrum. (b) An RSA spectrum, as obtained from a different drum with a less regular mode spectrum. Both electrical and shot noise terms are present in the background, where the former accounts for the slanted background.

order approximation is made for the variation of these parameters with the displacement. Of particular interest is the optical frequency shift per displacement $G \equiv \partial\omega_c/\partial x$, and the vacuum optomechanical coupling strength g_0 that is associated with such dispersive coupling [17]:

$$g_0 \equiv Gx_{zpf} = \sqrt{\frac{\hbar}{2m_{\text{eff}}\Omega_m}} G. \quad (11)$$

Here, x_{zpf} is the amplitude of the mechanical zero-point fluctuations.

Following Eq. (1), mechanical fluctuation spectra such as that in Fig. 10(b) are obtained. It shows an example signal recorded on the RSA at a probe laser wavelength of 1498 nm. The mechanical mode of the drum is seen as a peak in the spectrum. Figure 10(c) shows the detected spectra on the RSA for different laser frequencies, showing a varying signal strength and also a shift in mechanical frequency. The structure is expected to downshift in frequency with increasing temperature as in Fig. 8(a), which is corroborated by our experiment as the shift varies as the coupling of light to the plasmon mode varies. We note however that the maximal frequency shift seems to occur approximately 2 THz away from the perceived optical resonance, which can be seen by comparing the optical resonance spectra with the mechanical frequency shift spectra. This behaviour is shown by other structures as well. This may be caused by a spectral variation of absorbance or mechanical interaction with the supports, which may lead to additional stresses that cause an additional frequency shift with deposited power. Of further note is that we observe that the wavelength of maximum transduction can differ slightly from one mechanical mode to another, as we report in Supplement 1 section 5.

Assuming a thermal motion spectral density, the derivative $\partial R/\partial x$ can be obtained from the spectra presented in Fig. 10(c) through

$$P_{\text{RSA}}(\Omega) = \frac{2.12 \text{ RBW}}{Z} |\zeta_{\text{AC}}|^2 P_{\text{in}}^2 \left(\frac{\partial R}{\partial x} \right)^2 S_{xx}^{\text{th}}(\Omega), \quad (12)$$

where RBW is the resolution bandwidth of the RSA and Z its impedance. The derivation of this formula, as well as how to obtain the values for these parameters, is outlined in Supplement 1

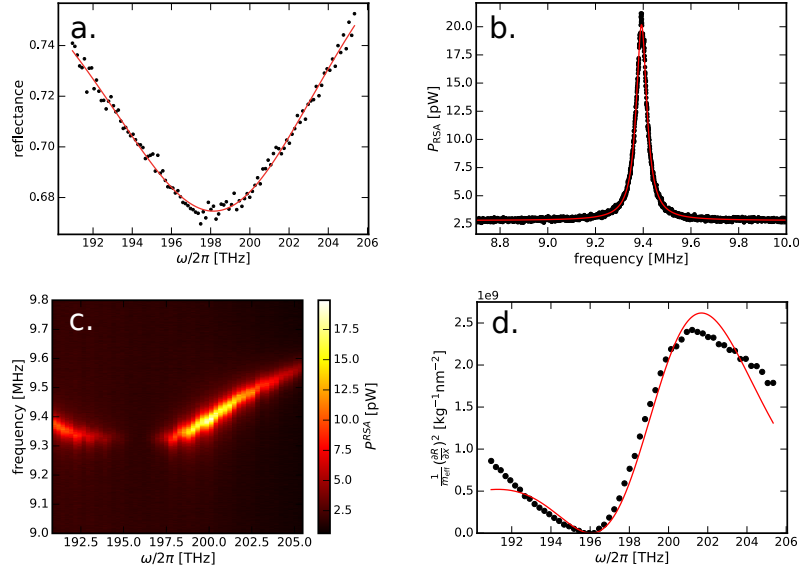


Fig. 10. (a) Optical reflectance of the drum shown in Fig. 9(b). The fitted parameters have values of $\kappa_0/2\pi = 16.2$ THz, $\omega_c/2\pi = 198.8$ THz, $\kappa_{ex}/2\pi = 0.8$ THz, $r_0 = 0.91$, $\varphi = -0.14$ rad. (b) Single power spectrum of the signal, obtained using a probe laser at 1498 nm and a probe power of 690 μ W. (c) Signal strength and mechanical frequency as a function of optical frequency. (d) Partial derivative of reflectance with respect to position as a function of optical frequency. The model is fitted to this data with a red line.

section 3. As such, the frequency-integrated signal under the peak is

$$\int P_{\text{RSA}}(\Omega)d\Omega = \frac{1.06 \text{ RBW}}{Z} |\zeta_{\text{AC}}|^2 P_{\text{in}}^2 \frac{1}{m_{\text{eff}}} \left(\frac{\partial R}{\partial x} \right)^2 \frac{k_{\text{B}}T}{\Omega}, \quad (13)$$

where we note that the integration runs over all positive frequencies. In Fig. 10(d), the derived values of $m_{\text{eff}}^{-1}(\partial R/\partial x)^2$ are shown as a function of laser wavelength. The change of the parameters in Eq. (4) to displacement can be estimated by fitting that equation to the transduction strength spectrum shown in Fig. 10(d), where each of the derivatives with respect to position is fitted as a constant, due to our linear approximation. This yields the values shown in Table 1 for this specific structure. We note that in comparison to the values expected from simulations (Fig. 4), the experimentally estimated modulation of intrinsic optical losses (due to absorption and scattering to other modes) $\partial\kappa_0/\partial x$ is relatively large. While the precise reason is not known, we remark that the fact that our model assumes a single Lorentzian response is a significant simplification: Because of the finite angular spread of the beam and finite size of the grating, multiple bands are effectively probed simultaneously. Nonetheless, taking the measured value of dispersive coupling $x_{\text{zpf}}^{-1/2}(\partial\omega_c/\partial x)$, the vacuum optomechanical coupling strength for this mode can be readily estimated by multiplying with $\sqrt{\hbar/(2\Omega_m)}$ in line with Eq. (11), giving $g_0/2\pi = 11.4$ MHz.

3.2.3. Characterization of plasmonic force

We next turn to characterizing actuation of the membrane resonator through plasmon-induced forces. To this end, we perform a pump-probe experiment in which we illuminate the sample with a time-modulated drive laser at 1550 nm, while detecting the motion of the drum using a probe laser at 1480 nm. Assuming dispersive coupling to a single optical cavity (resonator), one expects the force exerted by the light on the mechanical resonator to equal $\hbar Gn$, where n

Table 1. Table showing the fitted values for the dependence of various parameters on position x . Another column is added with values for a realistic effective mass of the mechanical mode.

expression	relative value	value for $m_{\text{eff}} = 10 \text{ pg}$
$(2\pi\sqrt{m_{\text{eff}}})^{-1} (\partial\omega_c/\partial x)$	$1.93 \times 10^9 \text{ GHz}/(\text{nm}\sqrt{\text{kg}})$	193 GHz/nm
$(2\pi\sqrt{m_{\text{eff}}})^{-1} (\partial\kappa_0/\partial x)$	$-1.70 \times 10^9 \text{ GHz}/(\text{nm}\sqrt{\text{kg}})$	-170 GHz/nm
$(2\pi\sqrt{m_{\text{eff}}})^{-1} (\partial\kappa_{\text{ex}}/\partial x)$	$1.73 \times 10^7 \text{ GHz}/(\text{nm}\sqrt{\text{kg}})$	1.73 GHz/nm

is the cavity occupancy. Thus, we express the force exerted on the system by the drive laser as $F(t) = \xi n(t)$, where $n(t)$ is the drive laser cavity occupancy and ξ thus the force per excitation in the optical resonator. The plasmonic cavity occupancy is sinusoidally modulated at frequency Ω by modulating the drive laser intensity, which subsequently generates an oscillating force that drives the motion of the mechanical resonator according to

$$x(\Omega) = \chi_m(\Omega)F(\Omega), \quad (14)$$

with $\chi_m = m_{\text{eff}}^{-1}(\Omega_m^2 - \Omega^2 - i\Omega\Gamma_m)^{-1}$ the mechanical susceptibility and position and force now written in the Fourier domain. The induced motion is read out using the probe laser with power P_p . Since we are far in the bad-cavity regime, we can assume the cavity occupancy, and hence the force, to directly follow the modulation of the drive laser.

In order to study the linear response of the membrane to the applied force, a signal from port 1 of the VNA is sent to the IM, which modulates the drive laser around mean power P_0 , whilst the output voltage from detector PD-2, detecting the signal from the probe laser, is sent to port 2 of the VNA. The S-parameter S_{21} , defined as $S_{21}(\Omega) = V_2(\Omega)/V_1(\Omega)$ is expected to scale with the mechanical susceptibility as

$$|S_{21}| = |\zeta_2||\zeta_{\text{filter}}| \left| \frac{\partial R}{\partial x} \right| P_p \xi |\chi_m(-\Omega_0)| |\chi_{\text{IM}}| \bar{n}, \quad (15)$$

where

$$\bar{n} = \frac{P_0}{\hbar\omega_d} \frac{\kappa_{\text{ex}}}{\Delta_d^2 + \kappa^2/4} \quad (16)$$

is the mean drive cavity occupancy, and ζ_{filter} is the measured transmission of the wavelength filter, as detailed in [Supplement 1](#) section 4.

The measured S-parameter can be seen in [Fig. 11](#). From the magnitude of this measurement, we can quantify the force per plasmon (normalized to mass). The S-parameter shows a resonant mechanical response and demonstrates that the motion of the resonator is (partly) driven by the optical field. Measuring a VNA response on a flat mirror reference yields the value of $|S_{21}^{\text{ref}}| = |\zeta_2||\chi_{\text{IM}}|P_0$. Together with the directly measured constants ζ_{filter} , P_p , Ω_m , and Γ_m , as well as the values of $m_{\text{eff}}^{-1}(\partial R/\partial x)$, κ_{ex} , and κ that were determined in the previous section, this allows using [Eq. \(15\)](#) to obtain an estimate of $\xi/\sqrt{m_{\text{eff}}}$, i.e., the force per plasmon divided by the square root of the effective mass:

$$\frac{\xi}{\sqrt{m_{\text{eff}}}} = 2.07 \times 10^{-4} \frac{\text{N}}{\sqrt{\text{kg}}}. \quad (17)$$

It is interesting to compare this value to the case that the force would be solely associated with dispersive optomechanical coupling parametrized through G . The equivalent force per photon divided by the square root of the effective mass can be estimated from the value of g_0 that we had obtained:

$$\frac{\hbar G}{\sqrt{m_{\text{eff}}}} = g_0 \sqrt{2\hbar\Omega_m} = 1.28 \times 10^{-6} \frac{\text{N}}{\sqrt{\text{kg}}}. \quad (18)$$

This analysis shows that the actual force exerted on the system is two orders of magnitude larger than what would be expected from the optomechanical force, which we found earlier

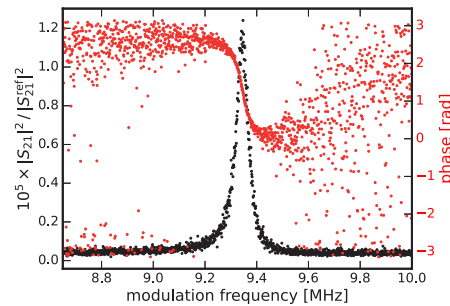


Fig. 11. A drive laser (29 μW oscillation amplitude) is used to drive the drum, while a probe laser (1136 μW at 1480 nm) is used for readout. The S-parameter shown here shows the response of the mechanical system to the modulation of the drive laser. It is expected to scale with the mechanical susceptibility of the resonator. The phase undergoes a π phase shift at resonance.

to closely approximate the electromagnetic force calculated from the Maxwell stress tensor. This discrepancy is too large to be understood from uncertainties in the estimated parameters. We thus conclude that another mechanism dominates the force induced by plasmonic fields on the resonator. The most likely explanation is a photothermoelastic effect, whereby the heating due to plasmon absorption in the gold membrane leads to a temperature gradient that induces stress actuating the motion of the drum resonator [64]. It would be interesting to systematically investigate this force and compare it to detailed calculations of the coupled optical, thermal, and mechanical fields [64]. Such a study, complemented by experimental measurements that study control over the photothermoelastic effect, e.g. by varying the thermal anchoring through design and by studying the effect for different devices spanning a large range of frequencies, could give useful insight in the various mechanisms at play, and the possible magnitude of photothermoelastic and radiation pressure forces in nanoplasmonic systems and derived sensors. This is however beyond the scope of the current study.

4. Discussion and outlook

In conclusion, we created a free-standing plasmonic gap waveguide system in which we demonstrated optical readout of the nanomechanical vibrations of metallic drum resonators. Efficient coupling to free space radiation allowed a displacement sensitivity of $\sim 10^{-14} \text{ m}/\sqrt{\text{Hz}}$ with near-infrared laser light. We identified incomplete release of the membranes as a fabrication challenge. Better control over the yield and mechanical performance could be realised by inducing controlled intrinsic stress in the membrane, through e.g. sputtering of metal films.

It was demonstrated that these structures can be optically driven by varying the intensity of a pump laser. The plasmonic forces were measured to be much larger (~ 100 times) than what is predicted from the optomechanical force, or from the Maxwell stress tensor. We postulate that this discrepancy may be caused by a large photothermoelastic effect that drives the mechanical motion. This is an interesting observation, in part because in other reports on actuation with nanoplasmonic fields the Maxwell stress tensor provided a more complete prediction of the observed magnitude [37]. We see that in different designs the force can not only be significantly enhanced beyond P/c , but also be multiple orders of magnitude larger due to photothermal coupling. This could in fact provide an interesting route for active optical manipulation of photonic properties, as well as coherent driving of resonators in sensing applications [10].

Indeed, the demonstrated transduction and actuation mechanisms could find specific application in nanomechanical sensing, as they provide size-matched, broadband, and efficient interfacing

with optical input and output fields. The relatively large active surface of metallic drum resonators could make them amenable to various applications in mass or pressure sensing. Mass sensing of trace gases nanoparticles, or proteins would benefit from having low-mass resonators with a large ‘capture area’. Optical actuation and readout provides an interesting alternative to electrical methods, where the required drive powers form a significant practical challenge [27]. The fact that the resonators feature significant metal (Au) surfaces facilitates functionalization with (thiol) chemistry to bind specific molecules. We note that the modest mechanical quality factors of ~100 reported here could be potentially improved by investigating different materials and specifically combinations of dielectric and metallic layers. The fact that plasmonic fields, and in particular nanoscale gaps, are also very good sensors of refractive index due to e.g. masses or adsorbing molecules could make hybrid mechanical and refractive index sensing especially appealing [65].

Funding. European Union Horizon 2020 Framework Programme (Grant Agreements No. 732894 (FET Proactive HOT) and No. 829067(FET Open THOR)); Nederlandse Organisatie voor Wetenschappelijk Onderzoek (NWO).

Acknowledgments. The authors thank R. Thijssen and R. Leijssen for experimental assistance, and A. F. Koenderink for critical reading of the manuscript.

Disclosures. The authors declare no conflicts of interest.

Data availability. Data underlying the results presented in this paper are not publicly available at this time but may be obtained from the authors upon reasonable request.

Supplemental document. See [Supplement 1](#) for supporting content.

References

1. L. Midolo, A. Schliesser, and A. Fiore, “Nano-opto-electro-mechanical systems,” *Nat. Nanotechnol.* **13**(1), 11–18 (2018).
2. P. S. Waggoner and H. G. Craighead, “Micro- and nanomechanical sensors for environmental, chemical, and biological detection,” *Lab Chip* **7**(10), 1238 (2007).
3. J. Arlett, E. Myers, and M. Roukes, “Comparative advantages of mechanical biosensors,” *Nat. Nanotechnol.* **6**(4), 203–215 (2011).
4. M. S. Hanay, S. Kelber, A. K. Naik, D. Chi, S. Hentz, E. C. Bullard, E. Colinet, L. Duraffourg, and M. L. Roukes, “Single-protein nanomechanical mass spectrometry in real time,” *Nat. Nanotechnol.* **7**(9), 602–608 (2012).
5. J. Tamayo, P. M. Kosaka, J. J. Ruz, and M. Calleja, “Biosensors based on nanomechanical systems,” *Chem. Soc. Rev.* **42**(3), 1287–1311 (2013).
6. M. S. Hanay, S. I. Kelber, C. D. O’Connell, P. Mulvaney, J. E. Sader, and M. L. Roukes, “Inertial imaging with nanomechanical systems,” *Nat. Nanotechnol.* **10**(4), 339–344 (2015).
7. K. Shiba, G. Imamura, and G. Yoshikawa, “Nanomechanical Sensors,” in *Biomaterials Nanoarchitectonics*, (Elsevier, 2016), pp. 177–196.
8. V. A. Aksyuk, “Sensing without power,” *Nat. Nanotechnol.* **12**(10), 940–941 (2017).
9. J. J. Ruz, O. Malvar, E. Gil-Santos, D. Ramos, M. Calleja, and J. Tamayo, “A Review on Theory and Modelling of Nanomechanical Sensors for Biological Applications,” *Processes* **9**(1), 164 (2021).
10. K. Ekinci, “Electromechanical Transducers at the Nanoscale: Actuation and Sensing of Motion in Nanoelectromechanical Systems (NEMS),” *Small* **1**(8-9), 786–797 (2005).
11. O. Basarir, S. Bramhavar, and K. L. Ekinci, “Motion Transduction in Nanoelectromechanical Systems (NEMS) Arrays Using Near-field Optomechanical Coupling,” *Nano Lett.* **12**(2), 534–539 (2012).
12. Y. T. Yang, C. Callegari, X. L. Feng, K. L. Ekinci, and M. L. Roukes, “Zeptogram-Scale Nanomechanical Mass Sensing,” *Nano Lett.* **6**(4), 583–586 (2006).
13. T. Larsen, S. Schmid, L. Grönberg, A. O. Niskanen, J. Hassel, S. Dohn, and A. Boisen, “Ultrasensitive string-based temperature sensors,” *Appl. Phys. Lett.* **98**(12), 121901 (2011).
14. D. Papas, J.-Y. Ou, E. Plum, and N. I. Zheludev, “Optomechanical metamaterial nanobolometer,” *APL Photonics* **6**(12), 126110 (2021).
15. D. López, R. S. Decca, E. Fischbach, and D. E. Krause, “MEMS-based force sensor: Design and applications,” *Bell Labs Tech. J.* **10**(3), 61–80 (2005).
16. F. Bemani, O. Cernotík, L. Ruppert, D. Vitali, and R. Filip, “Force Sensing in an Optomechanical System with Feedback-Controlled In-Loop Light,” *Phys. Rev. Appl.* **17**(3), 034020 (2022).
17. M. Aspelmeyer, T. J. Kippenberg, and F. Marquardt, “Cavity optomechanics,” *Rev. Mod. Phys.* **86**(4), 1391–1452 (2014).
18. Y.-W. Hu, Y.-F. Xiao, Y.-C. Liu, and Q. Gong, “Optomechanical sensing with on-chip microcavities,” *Front. Phys.* **8**(5), 475–490 (2013).
19. F. Liu, S. Alaie, Z. C. Leseman, and M. Hossein-Zadeh, “Sub-pg mass sensing and measurement with an optomechanical oscillator,” *Opt. Express* **21**(17), 19555 (2013).

20. A. Venkatasubramanian, V. T. K. Sauer, S. K. Roy, M. Xia, D. S. Wishart, and W. K. Hiebert, "Nano-Optomechanical Systems for Gas Chromatography," *Nano Lett.* **16**(11), 6975–6981 (2016).
21. E. Sage, M. Sansa, S. Fostner, M. Defoort, M. Gély, A. K. Naik, R. Morel, L. Duraffourg, M. L. Roukes, T. Alava, G. Jourdan, E. Colinet, C. Masselon, A. Brenac, and S. Hentz, "Single-particle mass spectrometry with arrays of frequency-addressed nanomechanical resonators," *Nat. Commun.* **9**(1), 3283 (2018).
22. Ramos Martín-Pérez and Calleja Tamayo, "Coherent Optical Transduction of Suspended Microcapillary Resonators for Multi-Parameter Sensing Applications," *Sensors* **19**(23), 5069 (2019).
23. F. Ricci, M. T. Cuairan, G. P. Conangla, A. W. Schell, and R. Quidant, "Accurate Mass Measurement of a Levitated Nanomechanical Resonator for Precision Force-Sensing," *Nano Lett.* **19**(10), 6711–6715 (2019).
24. M. P. Maksymowych, J. N. Westwood-Bachman, A. Venkatasubramanian, and W. K. Hiebert, "Optomechanical spring enhanced mass sensing," *Appl. Phys. Lett.* **115**(10), 101103 (2019).
25. B.-B. Li, L. Ou, Y. Lei, and Y.-C. Liu, "Cavity optomechanical sensing," *Nanophotonics* **10**(11), 2799–2832 (2021).
26. X. Liu, W. Liu, Z. Ren, Y. Ma, B. Dong, G. Zhou, and C. Lee, "Progress of optomechanical micro/nano sensors: a review," *Int. J. Optomechatronics* **15**(1), 120–159 (2021).
27. I. Bargatin, E. B. Myers, J. S. Aldridge, C. Marcoux, P. Brianceau, L. Duraffourg, E. Colinet, S. Hentz, P. Andreucci, and M. L. Roukes, "Large-Scale Integration of Nanoelectromechanical Systems for Gas Sensing Applications," *Nano Lett.* **12**(3), 1269–1274 (2012).
28. R. Thijssen, E. Verhagen, T. J. Kippenberg, and A. Polman, "Plasmon Nanomechanical Coupling for Nanoscale Transduction," *Nano Lett.* **13**(7), 3293–3297 (2013).
29. R. Thijssen, T. J. Kippenberg, A. Polman, and E. Verhagen, "Parallel Transduction of Nanomechanical Motion Using Plasmonic Resonators," *ACS Photonics* **1**(11), 1181–1188 (2014).
30. B. J. Roxworthy and V. A. Aksyuk, "Nanomechanical motion transduction with a scalable localized gap plasmon architecture," *Nat. Commun.* **7**(1), 13746 (2016).
31. B. J. Roxworthy and V. A. Aksyuk, "Electrically tunable plasmomechanical oscillators for localized modulation, transduction, and amplification," *Optica* **5**(1), 71 (2018).
32. A. N. Koya, J. Cunha, K. A. Guerrero-Becerra, D. Garoli, T. Wang, S. Juodkazis, and R. Proietti Zaccaria, "Plasmomechanical Systems: Principles and Applications," *Adv. Funct. Mater.* **31**(41), 2103706 (2021).
33. Q. Duan, Y. Liu, S. Chang, H. Chen, and J.-h. Chen, "Surface Plasmonic Sensors: Sensing Mechanism and Recent Applications," *Sensors* **21**(16), 5262 (2021).
34. M. R. Gonçalves, H. Minassian, and A. Melikyan, "Plasmonic resonators: fundamental properties and applications," *J. Phys. D: Appl. Phys.* **53**(44), 443002 (2020).
35. J.-Y. Ou, E. Plum, J. Zhang, and N. I. Zheludev, "An electromechanically reconfigurable plasmonic metamaterial operating in the near-infrared," *Nat. Nanotechnol.* **8**(4), 252–255 (2013).
36. P. Cencillo-Abad, E. Plum, E. T. F. Rogers, and N. I. Zheludev, "Spatial optical phase-modulating metadvice with subwavelength pixelation," *Opt. Express* **24**(16), 18790 (2016).
37. J.-Y. Ou, E. Plum, J. Zhang, and N. I. Zheludev, "Giant Nonlinearity of an Optically Reconfigurable Plasmonic Metamaterial," *Adv. Mater.* **28**(4), 729–733 (2016).
38. R. Gao, Y. He, D. Zhang, G. Sun, J.-X. He, J.-F. Li, M.-D. Li, and Z. Yang, "Gigahertz optoacoustic vibration in sub-5 nm tip-supported nano-optomechanical metasurface," *Nat. Commun.* **14**(1), 485 (2023).
39. R. Thijssen, T. J. Kippenberg, A. Polman, and E. Verhagen, "Plasmomechanical Resonators Based on Dimer Nanoantennas," *Nano Lett.* **15**(6), 3971–3976 (2015).
40. M.-H. Chien, J. Steurer, P. Sadeghi, N. Cazier, and S. Schmid, "Nanoelectromechanical position-sensitive detector with picometer resolution," *ACS Photonics* **7**(8), 2197–2203 (2020).
41. C. Haffner, A. Joerg, M. Doderer, F. Mayor, D. Chelladurai, Y. Fedoryshyn, C. I. Roman, M. Mazur, M. Burla, H. J. Lezec, V. A. Aksyuk, and J. Leuthold, "Nano-opto-electro-mechanical switches operated at CMOS-level voltages," *Science* **366**(6467), 860–864 (2019).
42. S. Schmid, K. Wu, P. E. Larsen, T. Rindzevicius, and A. Boisen, "Low-Power Photothermal Probing of Single Plasmonic Nanostructures with Nanomechanical String Resonators," *Nano Lett.* **14**(5), 2318–2321 (2014).
43. M. S. Rodrigues, J. Borges, and F. Vaz, "Plasmonic Strain Sensors Based on Au-TiO₂ Thin Films on Flexible Substrates," *Sensors* **22**(4), 1375 (2022).
44. X. Yang, Y. Liu, R. F. Oulton, X. Yin, and X. Zhang, "Optical Forces in Hybrid Plasmonic Waveguides," *Nano Lett.* **11**(2), 321–328 (2011).
45. J. Zhang, K. F. MacDonald, and N. I. Zheludev, "Optical gecko toe: Optically controlled attractive near-field forces between plasmonic metamaterials and dielectric or metal surfaces," *Phys. Rev. B* **85**(20), 205123 (2012).
46. H. Zhu, F. Yi, and E. Cubukcu, "Plasmonic metamaterial absorber for broadband manipulation of mechanical resonances," *Nat. Photonics* **10**(11), 709–714 (2016).
47. J.-Y. Ou, E. Plum, and N. I. Zheludev, "Optical addressing of nanomechanical metamaterials with subwavelength resolution," *Appl. Phys. Lett.* **113**(8), 081104 (2018).
48. J. Kohoutek, D. Dey, A. Bonakdar, R. Gelfand, A. Sklar, O. G. Memis, and H. Mohseni, "Opto-Mechanical Force Mapping of Deep Subwavelength Plasmonic Modes," *Nano Lett.* **11**(8), 3378–3382 (2011).
49. T. V. Raziman and O. J. F. Martin, "Internal optical forces in plasmonic nanostructures," *Opt. Express* **23**(15), 20143 (2015).

50. G. Volpe, R. Quidant, G. m. c. Badenes, and D. Petrov, "Surface plasmon radiation forces," *Phys. Rev. Lett.* **96**(23), 238101 (2006).
51. M. Righini, A. S. Zelenina, C. Girard, and R. Quidant, "Parallel and selective trapping in a patterned plasmonic landscape," *Nat. Phys.* **3**(7), 477–480 (2007).
52. M. Righini, G. Volpe, C. Girard, D. Petrov, and R. Quidant, "Surface plasmon optical tweezers: Tunable optical manipulation in the femtonewton range," *Phys. Rev. Lett.* **100**(18), 186804 (2008).
53. M. L. Juan, M. Righini, and R. Quidant, "Plasmon nano-optical tweezers," *Nat. Photonics* **5**(6), 349–356 (2011).
54. B. J. Roxworthy, K. D. Ko, A. Kumar, K. H. Fung, E. K. C. Chow, G. L. Liu, N. X. Fang, and K. C. Toussaint, "Application of Plasmonic Bowtie Nanoantenna Arrays for Optical Trapping, Stacking, and Sorting," *Nano Lett.* **12**(2), 796–801 (2012).
55. Y. Zhang, C. Min, X. Dou, X. Wang, H. P. Urbach, M. G. Somekh, and X. Yuan, "Plasmonic tweezers: for nanoscale optical trapping and beyond," *Light: Sci. Appl.* **10**(1), 59 (2021).
56. M. Ghorbanzadeh, S. Darbari, and M. K. Moravvej-Farshi, "Graphene-based plasmonic force switch," *Appl. Phys. Lett.* **108**(11), 111105 (2016).
57. B. J. Roxworthy, S. Vangara, and V. A. Aksyuk, "Subdiffraction Spatial Mapping of Nanomechanical Modes Using a Plasmomechanical System," *ACS Photonics* **5**(9), 3658–3665 (2018).
58. D. Woolf, M. Loncar, and F. Capasso, "The forces from coupled surface plasmon polaritons in planar waveguides," *Opt. Express* **17**(22), 19996 (2009).
59. M. P. van Exter, V. T. Tenner, F. van Beijnum, M. J. A. de Dood, P. J. van Veldhoven, E. J. Geluk, and G. W. 't Hooft, "Surface plasmon dispersion in metal hole array lasers," *Opt. Express* **21**(22), 27422–27437 (2013).
60. Z. Fang, Y.-R. Zhen, L. Fan, X. Zhu, and P. Nordlander, "Tunable wide-angle plasmonic perfect absorber at visible frequencies," *Phys. Rev. B* **85**(24), 245401 (2012).
61. L. Novotny and B. Hecht, *Principles of Nano-Optics* (Cambridge University Press, 2012), 2nd ed.
62. L. D. Landau and E. M. Lifshitz, *Statistical Physics*, vol. 5 of *Course of Theoretical Physics* (Pergamon Press, 1969), 2nd ed.
63. S. Collard and R. McLellan, "High-temperature elastic constants of gold single-crystals," *Acta Metall. Mater.* **39**(12), 3143–3151 (1991).
64. A. G. Primo, C. M. Kersul, R. Benevides, N. C. Carvalho, M. Ménard, N. C. Frateschi, P.-L. de Assis, G. S. Wiederhecker, and T. P. Mayer Alegre, "Accurate modeling and characterization of photothermal forces in optomechanics," *APL Photonics* **6**(8), 086101 (2021).
65. P. M. Kosaka, V. Pini, R. A. da Silva, M. U. González, D. Ramos, M. Calleja, and J. Tamayo, "Detection of cancer biomarkers in serum using a hybrid mechanical and optoplasmonic nanosensor," *Nat. Nanotechnol.* **9**(12), 1047–1053 (2014).